J. Fluid Mech. (2000), *vol.* 412, *pp.* 355–378. Printed in the United Kingdom

Three-dimensional oscillatory flow over steep ripples

By P. SCANDURA, G. VITTORI AND P. BLONDEAUX

Dipartimento di Ingegneria Ambientale, Università di Genova, Via Montallegro 1, 16145, Genova, Italy

(Received 22 February 1999 and in revised form 11 November 1999)

The process which leads to the appearance of three-dimensional vortex structures in the oscillatory flow over two-dimensional ripples is investigated by means of direct numerical simulations of Navier–Stokes and continuity equations. The results by Hara & Mei (1990*a*), who considered ripples of small amplitude or weak fluid oscillations, are extended by considering ripples of larger amplitude and stronger flows respectively. Nonlinear effects, which were ignored in the analysis carried out by Hara & Mei (1990*a*), are found either to have a destabilizing effect or to delay the appearance of three-dimensional flow patterns, depending on the values of the parameters. An attempt to simulate the flow over actual ripples is made for moderate values of the Reynolds number. In this case the instability of the basic two-dimensional flow with respect to transverse perturbations makes the free shear layer generated by boundary layer separation become wavy as it leaves the ripple crest. Then the amplitude of the waviness increases and eventually complex three-dimensional vortex structures appear which are ejected in the irrotational region. Sometimes the formation of mushroom vortices is observed.

1. Introduction

A model able to provide a complete and accurate description of the three-dimensional oscillatory flow induced by sea waves close to steep ripples is not available. However a detailed knowledge of this flow and in particular of the dynamics of the vortex structures generated by flow separation at ripple crests is necessary to understand important phenomena which take place close to the sea bottom, such as for example sediment transport. Indeed, flow visualizations along with an analysis of sediment trajectories (see among others Nielsen 1979) show that for typical field conditions, during the accelerating phases, it is the combined action of the attached boundary layer along the stoss side of the ripple and of the vortex structure generated by flow separation at the ripple crest that creates a small cloud of sediment just above the lee side of the ripple. Later, even though the flow decelerates, the vortex structure strengthens, the size of the recirculating cell increases and more sediment tends to be piled up at the ripple crest. Then the flow reverses and a lot of sediment is carried into suspension far from the bottom leaving the ripple profile at the crest, because it is trapped by the vortex structure which is convected by the local velocity. Later, the strength of the main vortex structure decays because of viscous effects and the gravity force prevails over drag forces and sediment is slowly released along the bed profile. In the meantime, a new vortex structure is generated and after half a wave period,

the flow and concentration distribution are the mirror images of those displayed at the beginning.

A traditional approach to describing particle dispersion in turbulence is to regard the phenomenon as a Fickian diffusion process. However, attempts to estimate the turbulent-exchange coefficient have not been successful and it has not been possible to establish any simple empirical relationship between this apparent turbulent-exchange coefficient and flow parameters. Since this kind of process is dominated by the convection of sediment by the vortex structures generated by the separation of the bottom boundary layer, it is our opinion that in order to describe the dynamics of sediment particles, it is first necessary to understand vorticity time development.

Some attempts to understand vorticity dynamics in an oscillatory flow close to a rippled bed have been performed by among others Sleath (1974), Sato, Mimura & Watanabe (1984), Longuet–Higgins (1981), Smith & Stansby (1985), Shum (1988), Blondeaux & Vittori (1991) (see also the works quoted in the above papers) by using finite-difference schemes, discrete vortex methods and pseudo-spectral approaches. The movement of sediment grains has been described by Hansen, Fredsøe & Deigaard (1994) who used a 'cloud-in-cell' method to determine the time development of the vortex structures generated by boundary layer separation and a Lagrangian approach to visualize sediment motion. However, all the above works assume the flow to be two-dimensional and therefore the breakdown of the two-dimensional vortices into smaller three-dimensional structures which eventually dissipate is not described. Hence, such models require heuristic approximations to bring the results into agreement with laboratory and field data.

A theoretical attempt to understand the process which leads to a three-dimensional flow over a two-dimensional bottom configuration has recently been made by Hara & Mei (1990*a*) who studied the hydrodynamic stability of the basic two-dimensional flow. To solve the problem by analytical means Hara & Mei (1990*a*) performed a linear analysis, i.e. they considered the time development of small (strictly infinitesimal) perturbations of the basic flow, and analysed two cases: case (i) is characterized by weak fluid oscillations over ripples of finite slope, case (ii) considers moderate fluid oscillations over ripples characterized by very gentle slope. Above some critical conditions, Hara & Mei (1990*a*) found that the basic flow is unstable with respect to three-dimensional spanwise perturbations because of the centrifugal forces induced by the curvature of the boundary layer (Taylor–Görtler instability). In case (i), the three-dimensional disturbances are localized in a small region close to ripple crests or ripple troughs depending on the parameters of the problem. In case (ii), three-dimensional perturbations grow which are spatially harmonic (periodic within one wavelength of the two-dimensional ripples) or subharmonic (periodic within twice the wavelength of the two-dimensional ripples) depending on the mode of instability.

Hara & Mei (1990*a*) suggest that the latter case is important to understand the process which leads to the appearance of brick-pattern ripples which are a bottom configuration characterized by long crests transverse to fluid motion and by longitudinal bridges spanning the ripple troughs. Indeed, Hara & Mei (1990*a*) showed that in case (ii) steady streaming is induced which would tend to accumulate sand particles in a pattern which suggests the initiation of brick-pattern ripples. Another possible mechanism leading to the formation of brick-pattern ripples was pointed out by Vittori & Blondeaux (1992). They showed that brick-pattern ripples can be originated by the simultaneous growth of two-dimensional and three-dimensional perturbations of the bottom which interact with each other with a mechanism similar to that described by Craik (1971) in a different context. As pointed out by Mei & Liu

(1993) and Blondeaux & Vittori (1999), the unstable modes considered by Hara & Mei (1990*a*) and those studied by Vittori & Blondeaux (1992) are not characterized by wavelengths of a different order of magnitude and in nature it is likely that the two mechanisms coexist, interact and complement each other. Hence, they should be combined for a full understanding of the process leading to brick-pattern ripple formation.

The results obtained by Hara & Mei (1990*a*) concerning the transition from a two-dimensional to a three-dimensional flow apply to ripples of small amplitude or to weak flows. For arbitrary values of the parameters, nonlinear effects are relevant and it is likely that the scenario of transition to a three-dimensional flow becomes richer and more complicated than that sketched by Hara & Mei (1990*a*). To have a better understanding of the dynamics of the three-dimensional vortex structures generated by the instability of the bottom boundary layer, in the present paper we compute the three-dimensional flow induced by an oscillating uniform pressure gradient close to a rippled bed. First, values of the parameters are considered close to those investigated theoretically by Hara & Mei (1990*a*). However, both fluid oscillations of large amplitude and large ripple heights are considered here such that the bottom boundary layer separates at the ripple crests and nonlinear effects are significant. The results obtained show that flow separation has a strong influence on the growth of three-dimensional perturbations of the basic two-dimensional flow field. In particular, nonlinear effects are found either to have a destabilizing effect or to delay the appearance of three-dimensional flow patterns, depending on the values of the parameters. The dynamics of the three-dimensional vortices are then investigated and the flow due to their interaction with the two-dimensional vortex structures is visualized and analysed. Finally, values of the parameters close to those characterizing actual sea ripples are considered. From knowledge of the velocity field, the dynamics of sediment grains and the time development of the bottom configuration can be inferred.

The structure of the rest of the paper is the following: in the next section the problem is formulated and the numerical procedure is presented. Then the basic two-dimensional oscillatory flow over steep ripples is briefly described by recovering some of the results of Blondeaux & Vittori (1991). In § 3, the appearance and development of three-dimensional perturbations is investigated and a comparison with the results by Hara & Mei (1990*a*) is made. In § 4, the numerical code is used to describe the three-dimensional oscillatory flow for values of the parameters typical of active ripples even though only moderate values of the Reynolds number are considered. The conclusions together with possible developments of the study are described in § 5.

2. The problem and the numerical approach

Let us consider the flow of an incompressible viscous fluid of density ρ^* and kinematic viscosity ν^*, above a two-dimensional wavy bottom which is rigid and smooth (hereinafter a star denotes dimensional quantities). The ambient fluid, far from the bottom, oscillates harmonically in the direction transverse to the crests of the waviness. As a reference, we define a Cartesian orthogonal coordinate system (x^*, y^*, z^*) with the y^*-axis pointing vertically upwards, the x^*- and z^*-axes normal and parallel to the ripple crests lying on a horizontal plane coincident with the average bottom as shown in figure 1.

Let us describe the ripple surface $y^* = F(x^*)$ parametrically by means of the

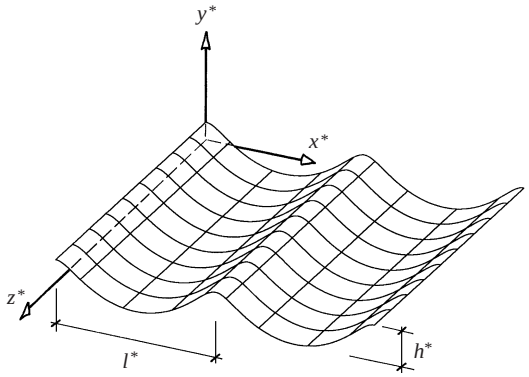

FIGURE 1. Sketch of the bottom configuration.

following relationships (Sleath 1984):

$$y^* = \frac{h^*}{2}\cos(k^*\xi^*), \qquad x^* = \xi^* - \frac{h^*}{2}\sin(k^*\xi^*), \tag{2.1}$$

where $k^* = 2\pi/l^*$ is the wavenumber of the waviness, h^* is its height and ξ^* is a dummy variable. As observed in real ripples, the bed profile (2.1) exhibits crests sharper than troughs (see figure 1).

The equations governing the fluid motion are written in terms of the orthogonal coordinate system (ξ^*, η^*, χ^*) defined by the following relationships (Sleath 1973):

$$\xi^* = x^* + \frac{h^*}{2}e^{-k^*\eta^*}\sin(k^*\xi^*), \qquad \eta^* = y^* - \frac{h}{2}e^{-k^*\eta^*}\cos(k^*\xi^*), \qquad \chi^* = z^*, \tag{2.2}$$

which map the bottom profile onto the plane $\eta^* = 0$. Moreover, the following dimensionless variables are introduced:

$$(\xi, \eta, \chi) = \frac{(\xi^*, \eta^*, \chi^*)}{(U_o^*/\omega^*)}, \qquad t = t^*\omega^*, \tag{2.3}$$

$$(v_\xi, v_\eta, v_\chi) = \frac{(v_\xi^*, v_\eta^*, v_\chi^*)}{U_0^*}, \qquad p = \frac{p^*}{\rho^*(U_0^*)^2}, \tag{2.4}$$

where t^* is time, $(v_\xi^*, v_\eta^*, v_\chi^*)$ are the velocity components along the ξ^*-, η^*-, χ^*-axes respectively and p^* is pressure. In (2.3), (2.4) U_0^* and ω^* are the amplitude and the angular frequency of fluid velocity oscillations far from the bottom respectively. The non-dimensional momentum and continuity equations read (Batchelor 1967, p. 588)

$$\begin{aligned}
&\frac{\partial v_\xi}{\partial t} + \frac{1}{J^{1/2}}\left[v_\xi\frac{\partial v_\xi}{\partial \xi} + v_\eta\frac{\partial v_\xi}{\partial \eta}\right] + v_\chi\frac{\partial v_\xi}{\partial \chi} - \frac{1}{2J^{3/2}}\left[v_\eta v_\xi\frac{\partial J}{\partial \eta} - v_\eta^2\frac{\partial J}{\partial \xi}\right] \\
&\quad = -\frac{1}{J^{1/2}}\frac{\partial p}{\partial \xi} + \frac{1}{Re}\left\{\frac{1}{J}\left[\frac{\partial^2 v_\xi}{\partial \xi^2} + \frac{\partial^2 v_\xi}{\partial \eta^2}\right] + \frac{\partial^2 v_\xi}{\partial \chi^2} - \frac{3}{4J^3}v_\xi\left[\left(\frac{\partial J}{\partial \xi}\right)^2 + \left(\frac{\partial J}{\partial \eta}\right)^2\right]\right. \\
&\qquad \left. + \frac{v_\xi}{2J^2}\left[\frac{\partial^2 J}{\partial \xi^2} + \frac{\partial^2 J}{\partial \eta^2}\right] + \frac{1}{J^2}\left[\frac{\partial v_\eta}{\partial \xi}\frac{\partial J}{\partial \eta} - \frac{\partial v_\eta}{\partial \eta}\frac{\partial J}{\partial \xi}\right]\right\},
\end{aligned} \tag{2.5}$$

$$\frac{\partial v_\eta}{\partial t}+\frac{1}{J^{1/2}}\left[v_\xi\frac{\partial v_\eta}{\partial \xi}+v_\eta\frac{\partial v_\eta}{\partial \eta}\right]+v_\chi\frac{\partial v_\eta}{\partial \chi}+\frac{1}{2J^{3/2}}\left[v_\eta v_\xi\frac{\partial J}{\partial \xi}-v_\xi^2\frac{\partial J}{\partial \eta}\right]$$
$$=-\frac{1}{J^{1/2}}\frac{\partial p}{\partial \eta}+\frac{1}{Re}\left\{\frac{1}{J}\left[\frac{\partial^2 v_\eta}{\partial \xi^2}+\frac{\partial^2 v_\eta}{\partial \eta^2}\right]+\frac{\partial^2 v_\eta}{\partial \chi^2}-\frac{3}{4J^3}v_\eta\left[\left(\frac{\partial J}{\partial \xi}\right)^2+\left(\frac{\partial J}{\partial \eta}\right)^2\right]\right.$$
$$\left.+\frac{v_\eta}{2J^2}\left[\frac{\partial^2 J}{\partial \xi^2}+\frac{\partial^2 J}{\partial \eta^2}\right]+\frac{1}{J^2}\left[\frac{\partial v_\xi}{\partial \eta}\frac{\partial J}{\partial \xi}-\frac{\partial v_\xi}{\partial \xi}\frac{\partial J}{\partial \eta}\right]\right\}, \tag{2.6}$$

$$\frac{\partial v_\chi}{\partial t}+\frac{1}{J^{1/2}}\left[v_\xi\frac{\partial v_\chi}{\partial \xi}+v_\eta\frac{\partial v_\chi}{\partial \eta}\right]+v_\chi\frac{\partial v_\chi}{\partial \chi}=-\frac{\partial p}{\partial \chi}+\frac{1}{Re}\left\{\frac{1}{J}\left[\frac{\partial^2 v_\chi}{\partial \xi^2}+\frac{\partial^2 v_\chi}{\partial \eta^2}\right]+\frac{\partial^2 v_\chi}{\partial \chi^2}\right\}, \tag{2.7}$$

$$\frac{1}{J^{1/2}}\left[\frac{\partial v_\xi}{\partial \xi}+\frac{\partial v_\eta}{\partial \eta}\right]+\frac{\partial v_\chi}{\partial \chi}+\frac{1}{2J^{3/2}}\left[v_\xi\frac{\partial J}{\partial \xi}+v_\eta\frac{\partial J}{\partial \eta}\right]=0, \tag{2.8}$$

where J is the Jacobian of transformation (2.2):

$$J=1+\left(\frac{hk}{2}\mathrm{e}^{-k\eta}\right)^2-2\frac{hk}{2}\mathrm{e}^{-k\eta}\cos(k\xi) \tag{2.9}$$

and Re is the flow Reynolds number defined as

$$Re=\frac{(U_0^*)^2}{\nu^*\omega^*}. \tag{2.10}$$

The problem is then closed by boundary conditions which force the fluid to oscillate harmonically far from the bottom

$$\lim_{\eta\to\infty}(v_\xi,v_\eta,v_\chi)=(\sin(t),0,0) \tag{2.11}$$

and to be at rest along the ripple profile

$$(v_\xi,v_\eta,v_\chi)=(0,0,0)\quad\text{for}\quad\eta=0. \tag{2.12}$$

The problem formulated above is solved numerically in a rectangular box following a procedure which makes use of finite-difference approximations and is a variant of the fractional-step method described for example in Kim & Moin (1985), Orlandi (1989) and Vittori & Verzicco (1998). The quantities L_ξ, L_η and L_χ denote box sizes in the ξ-, η- and χ-directions respectively. Since an integer number of ripple wavelengths is simulated, periodic boundary conditions are forced along the ξ-direction. Periodicity is also forced in the transverse direction χ, which is assumed to be a homogeneous direction. Finally, at the upper face of the computational box it has been assumed that

$$v_\eta=0,\qquad\frac{\partial v_\xi}{\partial \eta}=\frac{\partial v_\chi}{\partial \eta}=0. \tag{2.13}$$

As described in Kim & Moin (1985), the fractional-step method is an approximation of evolution equations based on the decomposition of the operators they contain. In applying it to Navier–Stokes equations, the role of the pressure term is to project an arbitrary vector field onto a divergence-free vector field. Using a two-step time

advancement scheme, the finite counterpart of equations (2.5)–(2.8) can be written as

$$\frac{\hat{v}_i - v_i^n}{\Delta t} = \tfrac{1}{2}(3H_i^n - H_i^{n-1}) - G_i(p^n) + \frac{1}{2R_e}[L_i(\hat{v}_i) + L_i(v_i^n)], \tag{2.14}$$

$$\frac{v_i^{n+1} - \hat{v}_i}{\Delta t} = -G_i(\phi^{n+1}), \tag{2.15}$$

with

$$\mathrm{D}(v_i^{n+1}) = 0. \tag{2.16}$$

In (2.14)–(2.16), v_i represents one of the velocity components along the orthogonal axes (ξ, η, χ), the indices n and $n+1$ refer to the values which the variables assume at time $t_n = n\Delta t$ and $t_{n+1} = (n+1)\Delta t$ respectively and the hat symbol indicates an intermediate velocity field which in general is not divergence free. Moreover, H_i represents the convective terms, while L_i and G_i represent the discrete finite-difference operators describing the viscous terms and the gradient of a scalar quantity along the three orthogonal axes. Finally, D is the finite-difference operator of the divergence of a vector quantity. It is worth pointing out that the operators H_1 and H_2 also contain parts of the viscous terms which are

$$\left[\frac{\partial v_\eta}{\partial \xi}\frac{\partial J}{\partial \eta} - \frac{\partial v_\eta}{\partial \eta}\frac{\partial J}{\partial \xi}\right] \Big/ (ReJ^2) \quad \text{and} \quad \left[\frac{\partial v_\xi}{\partial \eta}\frac{\partial J}{\partial \xi} - \frac{\partial v_\xi}{\partial \xi}\frac{\partial J}{\partial \eta}\right] \Big/ (ReJ^2)$$

respectively. The scheme outlined in (2.14)–(2.16) uses the second-order-explicit Adams–Bashforth scheme for the terms H_i and the second-order-implicit Crank–Nicholson scheme for the terms L_i. Implicit treatment of the viscous terms eliminates the numerical viscous stability restriction which may be particularly severe close to the wall where a stretched mesh is used. Indeed, to have a better description of the velocity gradients which are larger close to the wall, the coordinate $\tilde{\eta}$ is introduced

$$\tilde{\eta} = ln\left(\frac{\eta + a}{a}\right) \tag{2.17}$$

(a is a stretching parameter to be fixed suitably) and a uniform grid spacing is used along $\tilde{\eta}$. The staggered grid shown in figure 2 is used (Harlow & Welch 1965). The momentum equations are evaluated at velocity nodes while continuity is enforced at the centre of each cell. One important advantage of using a staggered mesh for incompressible flows is that *ad hoc* pressure boundary conditions are not required. All the spatial derivatives in the momentum equations are approximated with second-order central finite differences.

To determine $\hat{v}_i$ by means of equation (2.14), the inversion of large sparse matrices is required. However, using an approximate factorization technique, equation (2.14) can be reduced to a tridiagonal form with a significant reduction in computing cost and memory (Kim & Moin 1985). Finally, the pressure field is computed using the relationship

$$p^{n+1} = p^n + \phi^{n+1} - \frac{\mathrm{D}(\hat{v}_i)}{2Re}, \tag{2.18}$$

once the scalar ϕ^{n+1} is determined by means of the Poisson equation derived combining (2.14)–(2.16). The Poisson equation is solved by using a spectral method in the χ-direction and finite-difference approximations in the ξ- and η-directions. Indeed, because periodic boundary conditions are forced in the χ-direction, the function ϕ^{n+1}

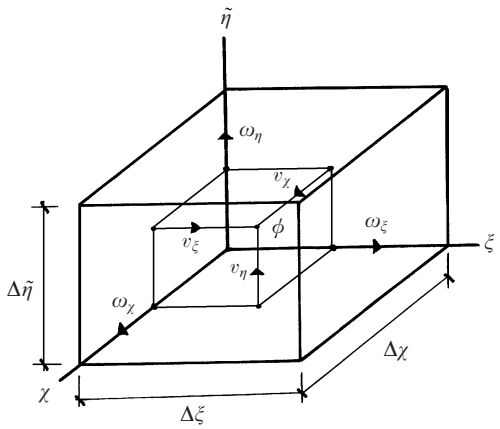

FIGURE 2. Sketch of the numerical grid.

is expanded in the form

$$\phi^{n+1} = \sum_{m=-M}^{M} \phi_m^{n+1}(\xi, \eta) e^{ik_m \chi}. \tag{2.19}$$

By approximating the spatial derivatives appearing in the equation for ϕ_m^{n+1} with their finite counterparts, linear algebraic bandwidth systems are derived which can be solved by means of a Gauss elimination approach. All the computations have been carried out on a workstation powered by an alpha-600 processor.

To test the reliability and the accuracy of the numerical code, results have been obtained by forcing the flow to be two-dimensional and comparing the numerical predictions with previous numerical simulations and analytical solutions. Good agreement is found when the present results are compared with those by Blondeaux & Vittori (1991) who solved the two-dimensional case using the vorticity–stream function formulation. Indeed, the plots shown in figure 3, where the time development of vorticity during a cycle is shown for $l = 1.333$, $h = 0.2$, $Re = 1250$, do not differ from those shown in figure 6 of Blondeaux & Vittori's (1991) paper. The present results have been obtained with $N_\xi = 120$, $N_\eta = 120$, $L_\eta = 1.333$ and $a = 0.136$ (N_ξ, N_η and N_χ denote the number of grid points in the ξ-, η- and χ-directions respectively). The dynamics of the vorticity, which is typical of ripples under sea waves, can be summarized as follows. At the beginning, clockwise vorticity is generated along the bed profile and in particular at the crests of the ripple. Increasing t, the boundary layer thickens on the downstream side of the crest till the flow separates (figure 3*c*). Then the vorticity rolls up and creates a well-defined vortex structure. In the second half of the cycle, the main vortex structure is no longer reinforced but it is simply convected away by local velocity. Meanwhile, the counterclockwise vorticity, which is induced by the combined action of the free-stream flow and of the clockwise vortex structure, creates a new vortex which couples with the old one forming a vortex pair which travels away because of the self-induced velocity. Then further counterclockwise vorticity is generated and when the flow reverses its direction again a new vortex is present near the crest and the phenomenon repeats similarly. These main features of vorticity dynamics are characteristic of steep ripples and large fluid displacement oscillations and were described by Longuet–Higgins (1981), Smith & Stansby (1985) and other authors.

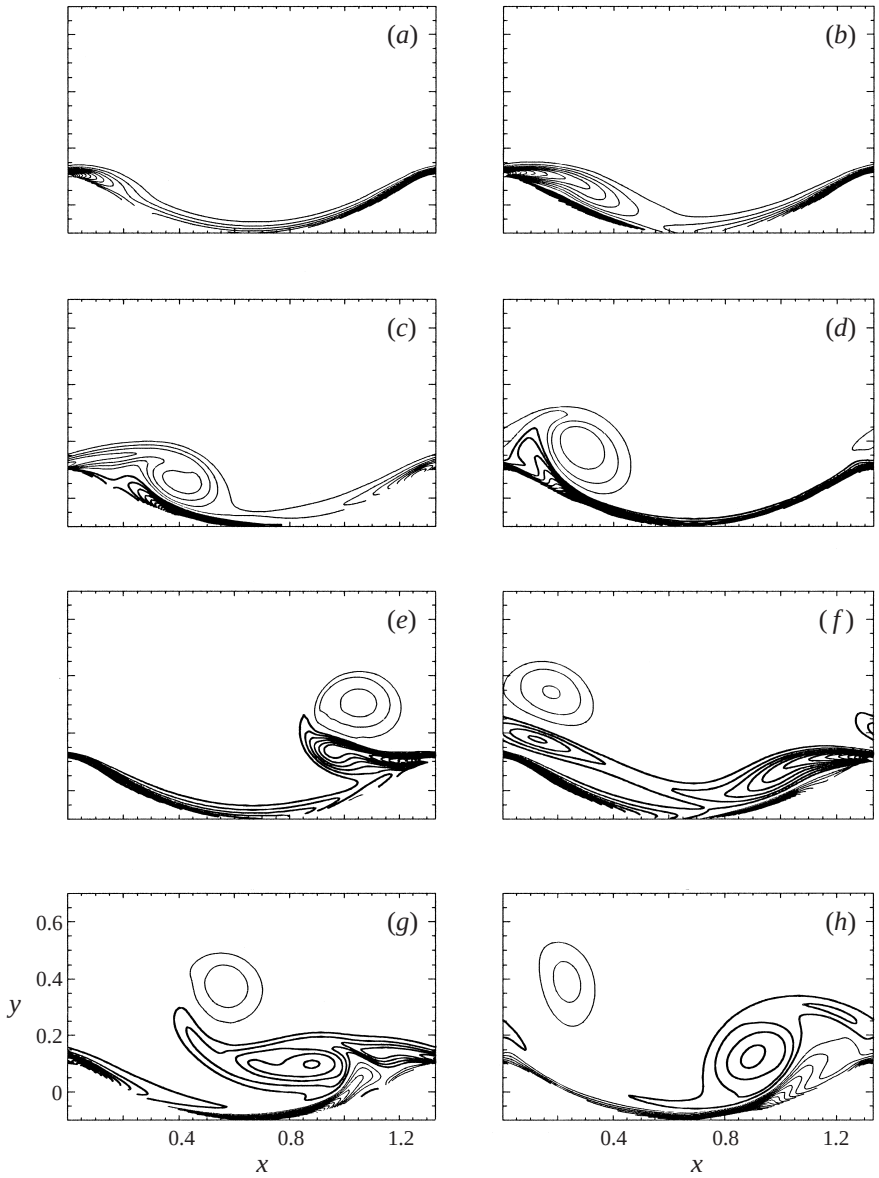

FIGURE 3. Spanwise vorticity time development for $l = 1.333$, $h = 0.2$, $Re = 1250$. Here and in all subsequent similar figures the thinner lines denote clockwise vorticity and the thicker lines anticlockwise. Here $\Delta\omega_\chi = 3.75$. (*a*) $t = \pi/4$, (*b*) $t = \pi/2$, (*c*) $t = 3\pi/4$, (*d*) $t = \pi$, (*e*) $t = 5\pi/4$, (*f*) $t = 3\pi/2$, (*g*) $t = 7\pi/4$, (*h*) $t = 2\pi$.

Good agreement has also been found between the present results and the analytical solutions by Vittori (1989), Blondeaux (1990) and Hara & Mei (1990*b*). An example is shown in figure 4 where the computed steady streaming induced by a weak oscillatory flow over steep ripples is plotted for $l = 20.96$, $h = 3.333$, $Re = 100$ along with the results obtained by Hara & Mei (1990*b*) who assumed infinitesimal values of the ratio $U_0^*/(\omega^* l^*) = 1/l$ between the amplitude of fluid displacement oscillations and ripple wavelength. The present values of the stream function ψ are numerically obtained using the relationship $v_\xi = (\partial\psi/\partial\eta)/\sqrt{J}$. The results plotted in figure 4 are

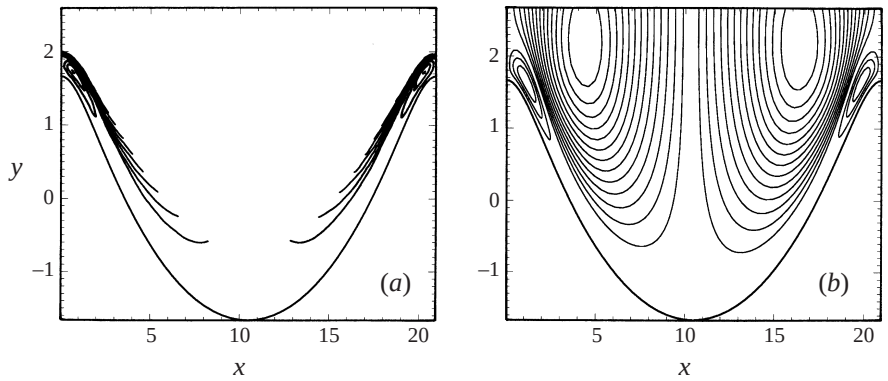

FIGURE 4. Steady component of the stream function ψ for $l = 20.96$, $h = 3.333$, $Re = 100$. (a) Hara & Mei's (1990b) results, (b) present results ($\Delta\psi = 0.00628$).

for the following values of the parameters of the numerical code $N_\xi = 64$, $N_\eta = 64$, $L_\eta = 20.96$, $a = 0.110$ and the simulation has been carried out up to 19 cycles. Even though the present results and those obtained by Hara & Mei (1990b) agree well from a qualitative point of view, there is some discrepancy when a quantitative comparison is made. The overall good accuracy of the numerical approach results from the following points: (i) the results of figure 4 are obtained for $1/l$ equal to about 0.048; (ii) the present results come from the solution of the full problem; (iii) the perturbation expansion used by Hara & Mei (1990b), which is based on the assumption of infinitesimal values of $1/l$, is truncated after two terms and ignores contributions of $O(1/l^2)$; (iv) the steady stream function plotted in figure 4 is of $O(1/l)$. Therefore, the results of figure 4(a) are expected to differ from those of figure 4(b) by an amount of order $1/l^2$, because of the terms ignored in Hara & Mei's (1990b) analysis. A quantitative comparison between figures 4(a) and 4(b) shows that relative differences of about 5% are present. Taking into account that the steady component of the stream function is of order $1/l$, it can be safely concluded that the relative error of the numerical approach is of $O(10^{-2}/l)$, i.e. $O(10^{-3})$.

3. Instability of the basic two-dimensional flow

Up to now the flow has been assumed two-dimensional and the χ-component of velocity has been inhibited in the numerical code. However, the theoretical investigation by Hara & Mei (1990a) shows that the two-dimensional oscillatory flow over a rippled bed may be unstable with respect to three-dimensional perturbations and a three-dimensional flow can develop. By analysing weak fluid oscillations over ripples of finite slope (case (i)), Hara & Mei (1990a) found that three-dimensional disturbances can grow which are localized in a small region either along the crests or along the troughs depending on ripple slope. When finite fluid oscillations are considered and the ripple slope is small (case (ii)), the region affected by flow instability becomes comparable with ripple wavelength and disturbances along adjacent ripples interact with each other. Both in case (i) and in case (ii), the parameters of the problem were chosen by Hara & Mei (1990a) in such a way that nonlinear effects are weak and the basic flow does not separate from ripple crests. Since boundary layer separation is one of the peculiar characteristics of the oscillatory flow over actual ripples, one of the main aims of the present work is to investigate how the results described by Hara & Mei (1990a) change when flow separates at ripple crests and nonlinear terms are not negligible.

Let us start by considering values of the parameters close to those of case (ii), i.e. finite values of the ratio between the amplitude of fluid displacement oscillations and ripple wavelength, but let us remove the assumptions introduced by Hara & Mei (1990*a*) of infinitesimal ripple steepness and infinite values of the Reynolds number. In this case the analysis by Hara & Mei (1990*a*) suggests that both spatially harmonic and subharmonic disturbances in the streamwise direction with respect to ripple wavelength can grow. Therefore, the size L_ξ of the computational box in the streamwise direction has been fixed equal to two ripple wavelengths. Because the results of different authors show that at a distance equal to l^* from the bottom, the flow differs by a small amount from the oscillating free-stream velocity, the dimensionless height L_η of the computational box has been fixed equal to l. Finally, different widths L_χ have been considered as discussed more widely in the following. If not otherwise specified 120 and 80 points have been used in the streamwise and vertical directions respectively and the stretching parameter a has been fixed in such a way that the first numerical cell has a height less than or equal to $0.1\,\delta^*$. The above number of grid points allows a fair description of the basic two-dimensional flow to be obtained. Indeed, by repeating some of the runs with a larger number ($N_\xi = 160$ and $N_\eta = 110$), it has been verified that the results presented in the following are not affected by the number of grid points. In all the runs the time step Δt has been fixed equal to 0.002. A few simulations have been repeated with $\Delta t = 0.001$ and no significant difference has been observed in the results.

The stability analysis by Hara & Mei (1990*a*) considers small (strictly infinitesimal) three-dimensional perturbations and hence different transverse modes evolve independently. In order to compare the present results with those of Hara & Mei (1990*a*), a first set of runs was performed using four points in the spanwise direction and varying L_χ in the range (0, 2.5). These runs mimic the growth of transverse perturbations characterized by a small amplitude and by a wavenumber in the χ-direction equal to $2\pi/L_\chi$. However, they cannot provide any information on the equilibrium flow configuration which is attained after the growth of the perturbations. Indeed, the presence of four points in the transverse direction allows only the three-dimensional disturbance with wavelength equal to L_χ to be simulated. When the perturbation attains a large amplitude, nonlinear effects would tend to generate ultraharmonic components which cannot be simulated. Tests performed with eight or 16 grid points in the transverse direction have shown that the use of four points allows reliable results to be obtained as long as the perturbation amplitude remains small. A similar approach was used by Akhavan, Kamm & Shapiro (1991) when studying the stability of the oscillatory boundary layer over a flat wall with respect to transverse perturbations characterized by a small amplitude. The results obtained for $l = 1.57$ and $Re = 2000$ are summarized in figure 5 where the abscissa is the transverse wavelength of the three-dimensional perturbations simulated by the code and the vertical coordinate is the quantity $T = h\sqrt{Re}/(2l^2)$ which is equal to the Taylor number of the basic flow as defined by Hara & Mei (1990*a*). It is recalled that the Taylor number measures the importance of centrifugal effects with respect to the viscous ones. The growth or decay of the perturbation, suitably inserted at the beginning of the simulation, has been judged by looking at the time behaviour of the specific energy E_χ, where E_χ is defined as

$$E_\chi(t) = \frac{1}{L_\chi L_\xi} \int_o^{L_\xi} \int_o^{L_\chi} \int_o^{L_\eta} v_\chi^2 J \, \mathrm{d}\chi \, \mathrm{d}\eta \, \mathrm{d}\xi. \tag{3.1}$$

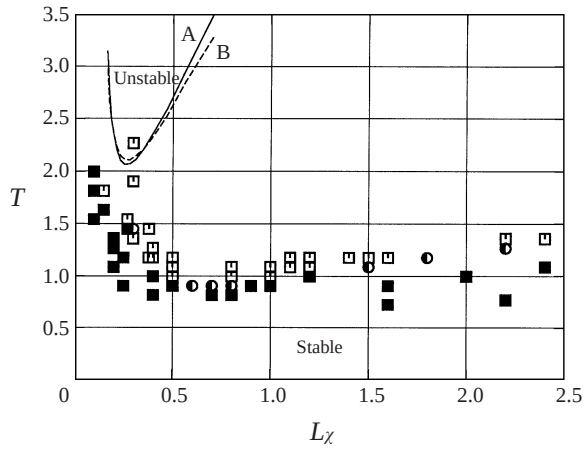

FIGURE 5. Stable ■, unstable □ and marginal ◐ two-dimensional oscillatory flows over small-amplitude ripples ($l = 1.57$, $Re = 2000$). Curves A and B are the theoretical marginal curves predicted by Hara & Mei (1990*a*) for mode 1-type II and mode 2-type III respectively.

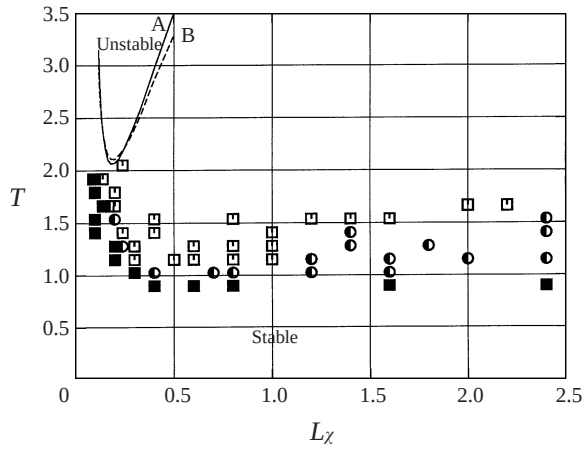

FIGURE 6. As figure 5 but for $Re = 4000$.

While for stable two-dimensional flows the value of E_χ tends rapidly to vanish, for the unstable ones E_χ grows and after a short time explodes because of the absence of the nonlinear effects able to damp the amplification of the perturbation. Some problems have been encountered in classifying runs characterized by values of the parameters close to the marginal conditions. In these cases, E_χ is characterized by a long transient during which large fluctuations take place. Hence, it turns out to be difficult to discriminate between stable and unstable conditions. To avoid any subjective judgement, in figure 5 the runs have been grouped in three classes. The first class is such that the value of E_χ after ten periods ($E_\chi(20\pi)$) is less than the initial value $E_\chi(0)$ divided by 5. The runs characterized by $E_\chi(20\pi)$ larger than $5E_\chi(0)$ belong to the second class. Lastly, runs such that $E_\chi(0)/5 < E_\chi(20\pi) < 5E_\chi(0)$ belong to the intermediate class. To compare the present simulations with Hara & Mei's (1990*a*) findings, the three sets of data have been classified as stable, unstable and marginal respectively even though these definitions should be treated with caution

for the reasons previously explained. To facilitate the comparison with the results by Hara & Mei (1990*a*), their theoretical curves for the most unstable modes are also plotted in figure 5. Curve A corresponds to the case defined by Hara & Mei (1990*a*) as mode 1-type II, while curve B is that of mode 2-type III. According to the analysis of Hara & Mei (1990*a*), when the Taylor number is larger than a critical value provided by curves A and B, the flow turns out to be unstable with respect to transverse perturbations which on the other hand decay when the Taylor number is smaller than its critical value. From figure 5 it clearly appears that the flow we are analysing is much more unstable than that considered by Hara & Mei (1990*a*). This finding can be explained by considering that the basic flow, the stability of which we are investigating, differs from that studied by Hara & Mei (1990*a*). In fact, to linearize Navier–Stokes equations and to work out the basic flow by analytical means, Hara & Mei (1990*a*) considered infinite values of Re and infinitesimal ripple slopes such that the quantity $h\sqrt{Re}/l^2$ is of order one. Here, a finite value of Re ($Re = 2000$) is considered, hence the ripple slope inducing the growth of transverse perturbations is not small and causes the separation of the basic two-dimensional flow at the ripple crest and the generation of large vortex structures. Lastly, for the largest values of h, the flow becomes chaotic through a Feigenbaum scenario (Feigenbaum 1978, 1979, 1980) as discussed by Vittori & Blondeaux (1991). In figure 6, results similar to those shown in figure 5 are plotted for $l = 1.57$ and $Re = 4000$. This set of runs is closer to Hara & Mei's (1990*a*) assumptions because of the larger value of Re. Comparing the results of figure 6 with those of figure 5, it appears that an increase of the Reynolds number makes the transition between stable and unstable flows move slightly towards the theoretical predictions by Hara & Mei (1990*a*). However, the present numerical results still significantly differ from the theoretical curves of Hara & Mei (1990*a*). No further attempt to find a better agreement by considering very large values of Re has been performed because for large values of the Reynolds number the flow is expected to become turbulent as discussed in Vittori & Verzicco (1998).

Some of the runs which have led to the results shown in figure 5 have been repeated by using 32 points in the spanwise direction, thus looking for the equilibrium configuration reached by the unstable flow. Results obtained with $N_\chi = 48$ are practically indistinguishable from the previous ones. In figure 7, the value of E_χ defined by (3.1) is shown versus time for $l = 1.57$, $Re = 2000$, $h = 0.12$, $L_\chi = 0.8$. It clearly appears that the energy of the perturbation, inserted at the beginning of the simulation, rapidly grows and attains a regime behaviour which is characterized by irregular fluctuations around an average value. The aperiodic behaviour of the perturbation is due to its nonlinear interaction with the basic flow. To gain an idea of the flow field which is set-up after the growth of the transverse perturbations, the vorticity component in the streamwise direction is computed and plotted in figure 8 at different phases during the cycle for a fixed value of y. The flow development is described during the 16th cycle when a steady oscillatory state is attained. However, for the sake of simplicity only the phase within the cycle is given in the figure caption. Perturbations, which are spatially subharmonic in the x-direction, are clearly detectable. Indeed, the spatial distribution of ω_x is characterized by patches which repeat every ripple, shifted in the χ-direction by $L_\chi/2$ between adjacent series. It is difficult to provide an exhaustive description of the flow since many three-dimensional small vortex structures appear which quickly evolve in time.

In obtaining these results the parameter $\alpha = 1/l$ introduced by Hara & Mei (1990*a*) and defined as the ratio between the amplitude of fluid displacement oscillations and ripple wavelength has been fixed equal to $2/\pi$. For such a value, the theoretical results

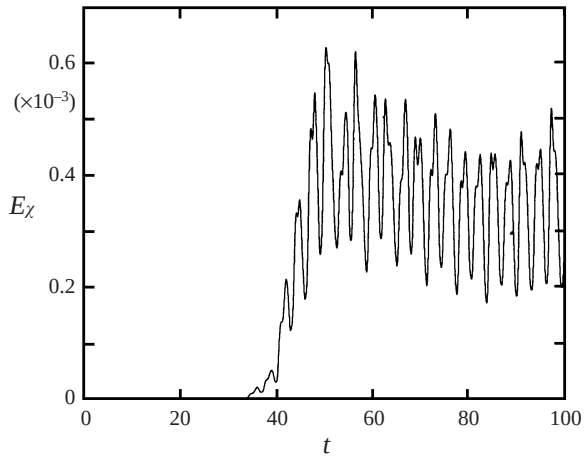

FIGURE 7. Time development of E_χ for $l = 1.57$, $h = 0.12$, $Re = 2000$, $L_\chi = 0.8$.

by Hara & Mei (1990*a*) suggest that the steady currents, which are set up by the growth of the three-dimensional perturbations, would tend to accumulate possible loose particles lying on a ripple surface in a pattern similar to that characterizing brick-pattern ripples. Even though the basic flow considered here differs from that studied by Hara & Mei (1990*a*) because of strong nonlinear effects, the qualitative conclusion given above is still valid. Indeed, from figure 9, which shows the distribution after a cycle of passive tracers uniformly released close to the bottom, it can be seen that particles are piled up close to ripple crests by the combined action of the attached flow on the stoss side of the ripple and of the vortex structure generated by boundary layer separation on the lee side. Particle drift in the ξ-direction is superposed on a slow movement in the spanwise direction which tends to create patches of low particle density along ripple troughs, which are L_χ apart. These patches are shifted by half a wavelength between adjacent troughs. Close to the borders of the low-density regions, particles tend to be piled up creating periodic patterns of longitudinal bridges, joining the crests of the ripples. As pointed out in the introduction, this particle pattern suggests that the centrifugal instability of the basic two-dimensional flow with respect to spatially subharmonic perturbations can play a role in the mechanism originating brick-pattern ripples.

The other case considered by Hara & Mei (1990*a*) (case (i)) is the stability of the flow induced close to steep ripples by weak fluid oscillations such that $1/l$ is much smaller than one and Re is of order l^2. In this case, Hara & Mei (1990*a*) showed that the disturbances which appear are localized in a small region along one ripple and gave the threshold of instability in terms of a local Taylor number T_L defined as $\sqrt{2}A_L^{*2}/(4\pi^2\delta^* R_L^*)$ where A_L^* is the amplitude of fluid displacement oscillations at the wall when viscous effects are ignored. Notice that the value of A_L^* varies along the ripple profile together with the local radius of curvature R_L^* of the bottom surface. Thus, the variation of the local Taylor number along the ripple surface is due to changes of both R_L^* and A_L^* which can be easily computed once ripple geometry is given.

An idea of the variation of the Taylor number along the ripple profile can be gained from figure 2 of Hara & Mei's (1990*a*) paper. For sufficiently large values of h^*/l^*, the absolute value of the positive maximum of T_L is much larger than that

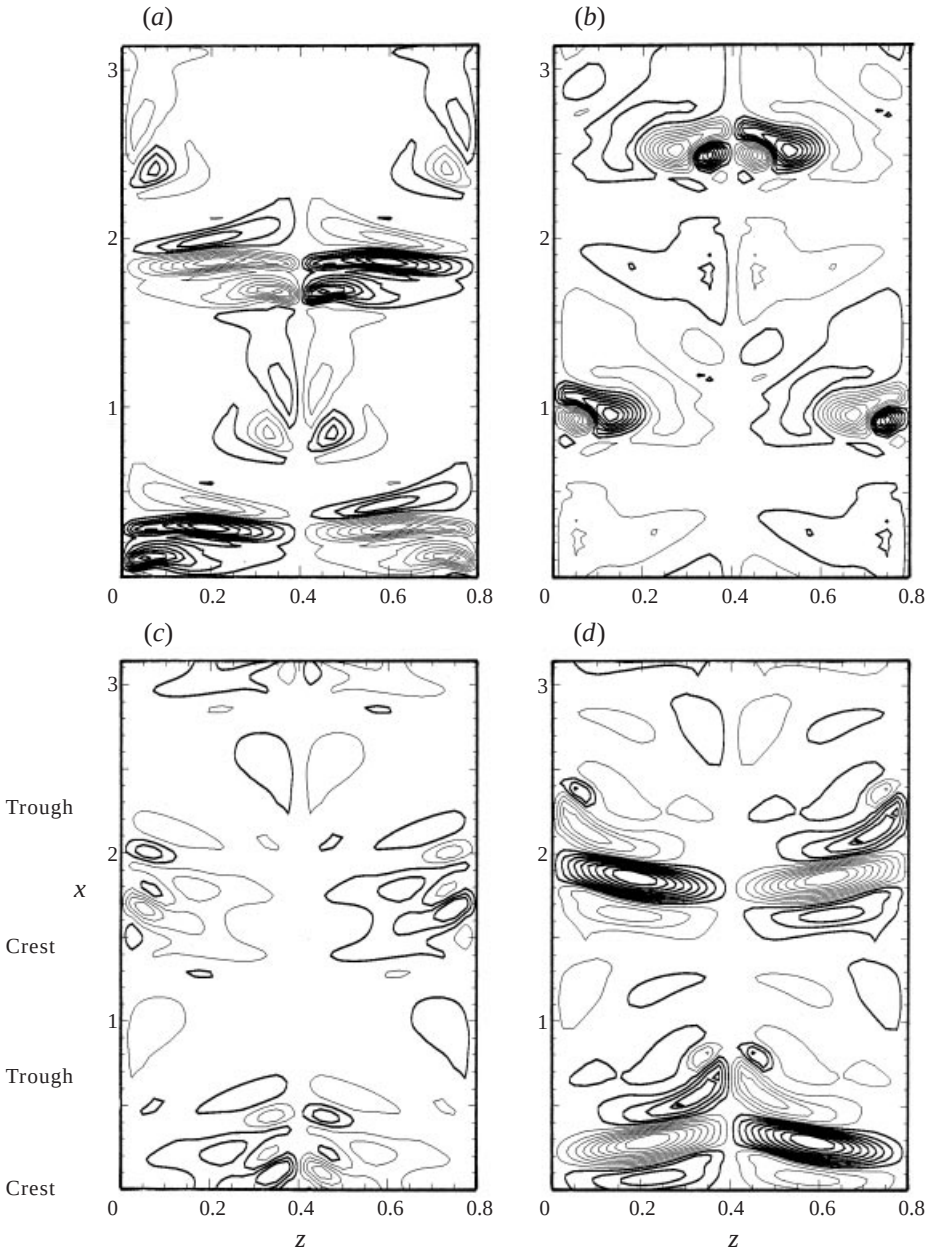

FIGURE 8. Plots of ω_x in the horizontal plane $y = 0.123$ for $l = 1.57$, $Re = 2000$, $h = 0.12$, $L_z = 0.8$. (*a*) $t = 0$; (*b*) $t = \pi/4$; (*c*) $t = \pi/2$; (*d*) $t = 3\pi/4$ ($\Delta\omega_x = 0.7$).

of the negative minimum and instability occurs first at the crest. This is of course because the crest has a sharper curvature than the trough for all but very small values of h^*/l^*. On the other hand, for very small h^*/l^* the absolute value of the Taylor number at the crests and at the troughs becomes equal and, as explained in Hara & Mei (1990*a*), instability occurs at the trough first. The flow for values of the parameters close to those considered by Hara & Mei (1990*a*) cannot be simulated by our code. In fact, as previously pointed out, Hara & Mei (1990*a*) assumed the

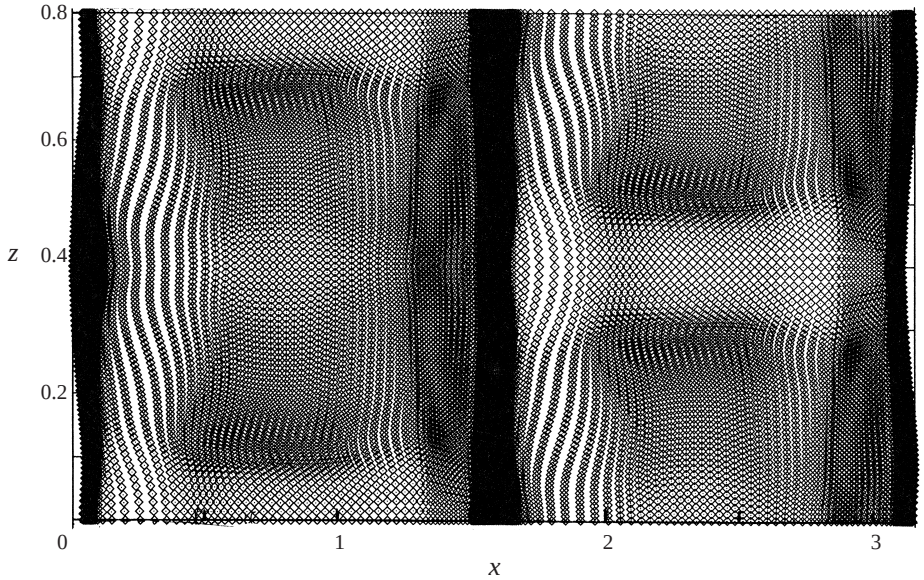

FIGURE 9. Position at $t = 34\pi$ of loose particles uniformly released close to the bottom at $t = 32\pi$ for $l = 1.57$, $Re = 2000$, $h = 0.12$, $L_\chi = 0.8$.

ripple wavelength l to be much larger than 1 and considered values of Re of order l^2. Attempts to satisfy the above conditions lead to thicknesses of the bottom boundary layer which are too small compared to ripple wavelength to be handled by numerical means. Moreover, for large values of Re the flow becomes turbulent and no agreement is expected between numerical simulations and the theoretical predictions by Hara & Mei (1990*a*).

However, the results obtained by Hall (1984), who studied the stability of the oscillatory flow around cylinders of circular section by assuming weak fluid oscillations and weak viscous effects, show that the growth of three-dimensional perturbations may be described fairly well by the theoretical analysis even when the amplitude of fluid oscillations U_o^*/ω^* becomes comparable with the radius r^* of the cylinder section. Indeed, the marginal conditions predicted by Hall (1984) compare very well with those determined experimentally by Honji (1975) even when $U_0^*/(\omega^* r^*)$ is about 1.5. Therefore, an attempt has been made to compare present numerical findings with the theoretical predictions by Hara & Mei (1990*a*) by considering finite values of ripple steepness but removing the assumptions of infinitesimal values of $1/l$ and values of Re of order l^2.

Since the theoretical analysis of Hara & Mei (1990*a*) suggests that the growth of the perturbations leads to the appearance of Görtler vortices localized around ripple crests and the vortices close to one crest do not interact with those originating around adjacent crests, the numerical simulations consider only one ripple wavelength. The ratio h/l was fixed equal to 0.12, while different values of Re and l were investigated to determine the region of instability in the plane (Re, $1/l$). The width of the computational box was fixed equal to $2\pi/(0.36\sqrt{Re})$ in order to simulate the growth of the most unstable modes as predicted by Hara & Mei (1990*a*). In a first set of runs, attention was focused on the linear growth of the three-dimensional perturbations and therefore four points in the transverse direction were used. Different values of N_ξ, N_η were employed depending on the values of the parameters of the problem. The

accuracy of the simulations was verified by repeating some of the computations with larger values of N_ξ and N_η. These simulations provided practically identical results. The criterion used to discriminate between stable and unstable runs is that previously described and based on the value assumed by the quantity E_χ after 10 cycles.

Figure 10 shows the simulations for which three-dimensional perturbations of the basic two-dimensional flow tend to decay and those such that three-dimensional perturbations grow. In figure 10 the abscissa is the Reynolds number while the vertical axis displays the quantity $1/l = U_0^*/(\omega^* l^*)$. According to Hara & Mei's (1990*a*) analysis, the plane $(Re, 1/l)$ can be divided in a stable region and an unstable one by curve A obtained by equating the local Taylor number at the crest to its critical value. For large values of l the flow is stable. When l is decreased and it becomes smaller than the critical value provided by curve A, the flow turns out to be unstable. The discrepancy between the results of Hara & Mei (1990*a*) and those of present numerical simulations is significant. However, in making the comparison it should be taken into account that in Hara & Mei's (1990*a*) analysis, the fluid displacement is supposed to be very small compared to ripple wavelength and the perturbations are supposed to evolve around ripple crests and to feel the radius of curvature of the crests only. On the other hand, for the simulations which have been carried out, the perturbations are convected along the ripple surface and feel different radii of curvature. To account for this fact, a new curve is drawn in figure 10 (curve B) which is obtained by defining an average value of the Taylor number equal to

$$\frac{h\sqrt{Re}}{2l^2}\frac{1}{2\pi}\int_0^{2\pi}\frac{\cos(\hat{\xi})-\pi(h/l)}{[1-2\pi(h/l)\cos(\hat{\xi})+\pi^2(h/l)^2]^{5/2}}\,\mathrm{d}\hat{\xi} \tag{3.2}$$

and equating it to the critical value. If the results of the numerical simulations are compared with curve B, the agreement is much better, in particular when large values of Re are considered.

The present numerical simulations show also that on decreasing the Reynolds number, the critical value of l decreases and the stable region widens and becomes larger than that predicted by Hara & Mei (1990*a*). In particular, for Re smaller than about 600 the flow appears to be stable whatever value of l is considered. Flow separation, which for fixed values of Re appears when small values of l are simulated, is the cause of the appearance of a stable region in the upper part of the $(Re, 1/l)$-plane. Indeed, for fixed values of the parameters of the problem, the curvature of the streamlines close to ripple crests is smaller for a separated flow than that characterizing an unseparated flow and hence the local Taylor number of a separated flow is smaller than that of an unseparated one. Therefore, transverse perturbations of separating flows damp out.

As previously pointed out, the runs shown in figure 10 have been performed using four points in the transverse direction to investigate the growth of the perturbations in the linear regime. Some of the runs have been repeated using 16 points in the transverse direction and 160, 120 in the streamwise and vertical directions respectively to describe the equilibrium attained by the flow after the growth of the transverse perturbations. By performing computations with $N_\chi = 32$, $N_\xi = 160$ and $N_\eta = 120$ it has been found that the differences are negligible. For example, the values of E_χ obtained during a cycle with $N_\chi = 32$ differ by a negligible amount from those obtained with $N_\chi = 16$. Similar results have been obtained by increasing N_ξ or N_η ($N_\xi = 200$, $N_\eta = 160$). Figures 11, 12 and 13 show the results for $Re = 875$, $l = 2.67$ and $L_\chi = 0.59$. It is worth pointing out that an analysis of the time

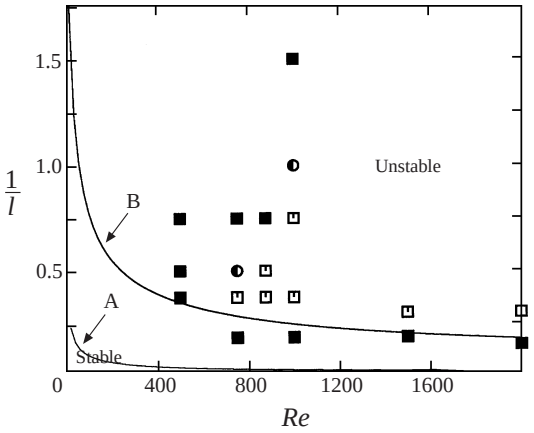

FIGURE 10. Stable ■, unstable □ and marginal ◐ two-dimensional oscillatory flows over steep ripples for $h/l = 0.12$. Curve A has been derived by Hara & Mei (1990*a*) for large values of l. Curve B is a heuristic adaptation of curve A.

development of the spanwise vorticity component shows that for these values of the parameters the viscous boundary layer remains attached to the ripple surface. The time behaviour of E_χ is plotted in figure 11 and shows that a steady oscillatory state is reached by the flow after about 45 cycles. From figure 12, where the streamwise component of vorticity ω_x is plotted at the same time in three vertical planes parallel to a ripple crest and close to it, it can be seen that the inception of a three-dimensional flow is associated with the appearance of Taylor–Görtler vortices. Indeed, the three-dimensional character of the flow is due to the presence of streamwise vorticity which is generated mainly around the crests where the radius of curvature is maximum. At the beginning of the simulation, the generation of streamwise vortices takes place during a small part of the cycle when the free-stream velocity is maximum. However, figure 13, where ω_x is plotted during the 45th cycle, shows that once generated, Taylor–Görtler vortices survive for more than half a cycle and are convected by the external velocity along the ripple surface, eventually leaving it at a ripple trough and originating a complex flow. Hence, for large times the generation of streamwise vorticity also takes place for phases different from $t = \pi/2$ and $t = 3\pi/2$.

4. Strong oscillatory flow over steep ripples

Up to now the growth of initially small three-dimensional perturbations of the two-dimensional oscillatory flow over ripples has been simulated by choosing the parameters of the problem close to the values analysed by Hara & Mei (1990*a*), even though some of their assumptions have been removed in order to investigate the effects of significant nonlinearity. In this section, we present some results obtained by fixing the parameters close to the values characterizing actual ripples even though only moderate values of the Reynolds number can be simulated. In particular, ripple steepness (h^*/l^*) has been fixed equal to 0.14 and the ratio between the amplitude of fluid displacement oscillations and ripple wavelength is set equal to 0.75, a value close to that observed in the field. Lastly, the Reynolds number is equal to 1005. Even though actual ripples are characterized by larger values of *Re*, we feel that the results obtained can provide useful information to help understand the flow generated by

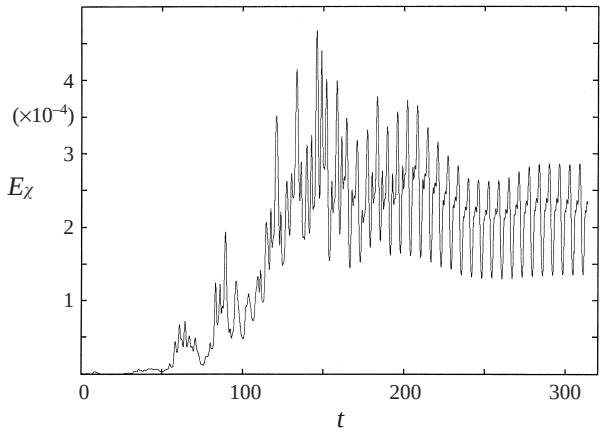

FIGURE 11. Time development of E_χ for $l = 2.67$, $h = 0.32$, $Re = 875$, $L_\chi = 0.59$.

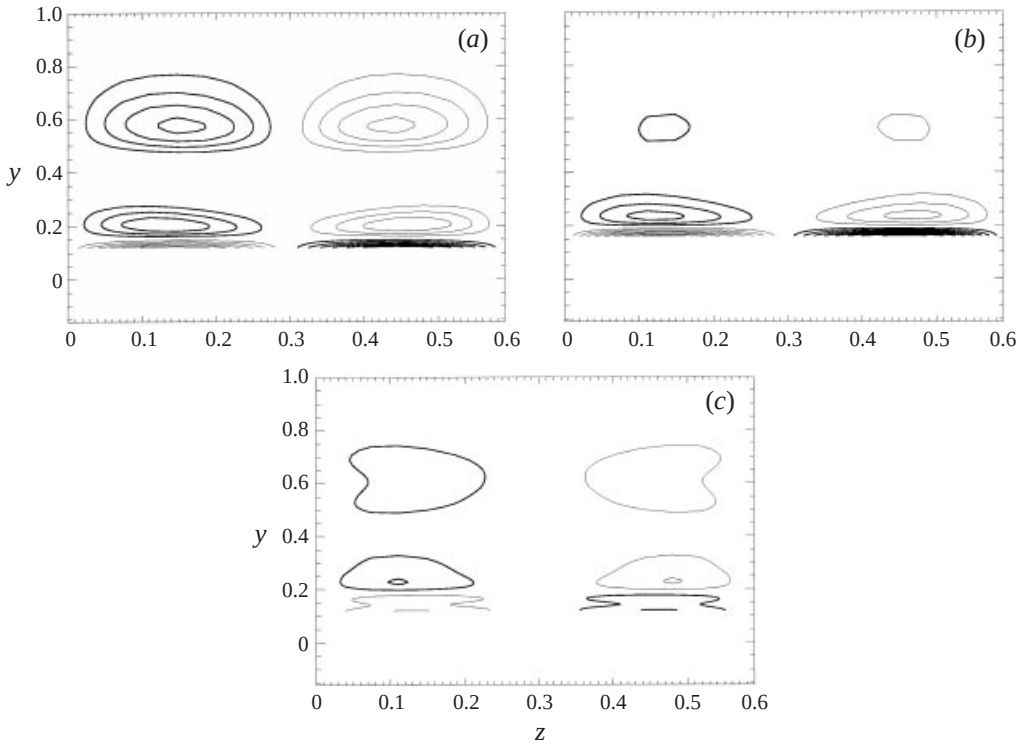

FIGURE 12. Streamwise component of vorticity ω_x for $l = 2.67$, $h = 0.12$, $Re = 875$, $L_\chi = 0.59$ at $t = \pi/2$ in the planes (*a*) $x = -0.20$; (*b*) $x = 0$; (*c*) $x = 0.20$ ($\Delta\omega_x = 0.07$).

sea waves close to a rippled bed. First, the width of the computational box in the spanwise direction has been fixed equal to 0.66 while L_ξ and L_η are equal to l. A perturbation periodic in the χ-direction with a wavelength equal to L_χ and a small amplitude was introduced at the beginning of the simulation. The value $L_\chi = 0.66$ was chosen because it is close to the wavelength of the transverse perturbations which are expected to be the most unstable according to Hara & Mei's (1990*a*) analysis.

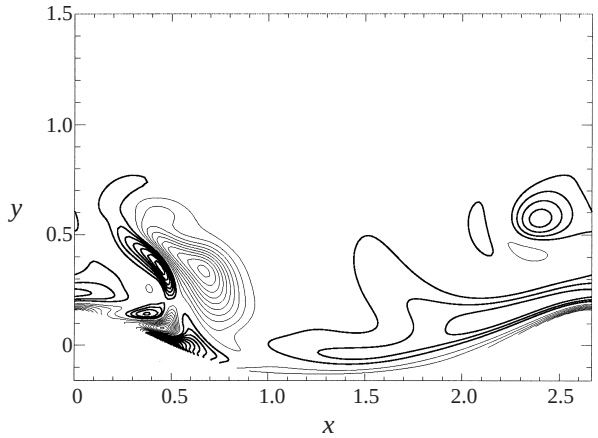

FIGURE 13. Streamwise component of vorticity ω_x for $l = 2.67$, $h = 0.32$, $Re = 875$, $L_\chi = 0.59$ in the plane $\chi = 0.11$ during the 15th period ($t = \pi/4$, $\Delta\omega_x = 0.2$).

The numerical code was run with $N_\xi = 64$, $N_\eta = 80$, $N_\chi = 32$ and a value of the stretching parameter such that the size of the first numerical cell is smaller than $0.1\delta^*$.

A preliminary investigation of the two-dimensional flow has shown that for these values of the parameters the flow is characterized by a chaotic behaviour (see the results described in Vittori & Blondeaux 1991). However, even though the velocity field does not repeat exactly after a wave period, the gross features of vorticity time development do not differ greatly from one cycle to the other. For this reason, in the following, the flow behaviour is described during the 14th cycle when a steady oscillatory state is attained by the flow and the value of t given in figure captions gives the phase within the cycle. In figure 14 the χ-component of vorticity is shown in a vertical plane characterized by $\chi = 0.33$ at different phases of the cycle. The formation of a vortex pair can be easily recognized similarly to the two-dimensional case (compare figure 14 with figure 3). However, the three-dimensional case is characterized by the formation of a three-dimensional vortex structure similar to a mushroom vortex. Indeed, the shear layer generated at the ripple crest becomes wavy in the χ-direction as it leaves the ripple crest. This behaviour is evident in figure 15(*a*) where ω_χ is plotted in a vertical plane parallel to ripple crests. The shear layer is close to the bottom for $\chi = 0$ and $\chi = L_\chi$, while in the middle of the computational cell it tends to leave the ripple surface. This behaviour is induced by the appearance of a significant component of vorticity in the streamwise direction which creates a vertical upwards motion of the fluid in the middle of the computational cell (see figure 15*b*). Ejection of vorticity towards the irrotational region is thus observed. Secondary velocity components also originate in a horizontal plane and the vortex pair is accelerated in the centre of the box and retarded at the sides. Of course, vorticity dynamics has a large influence on the convection of sediment and on erosion/deposition processes which control bottom morphology. To gain an idea of the trajectories of loose particles, in figure 16 the subsequent locations of passive tracers released at $t = 28\pi$ close to the ripple crest are plotted in the (x, z)-, (x, y)- and (y, z)-planes. It appears that the action of the vortex structure, created by boundary layer separation and the roll-up of vorticity, tend to lift particles from

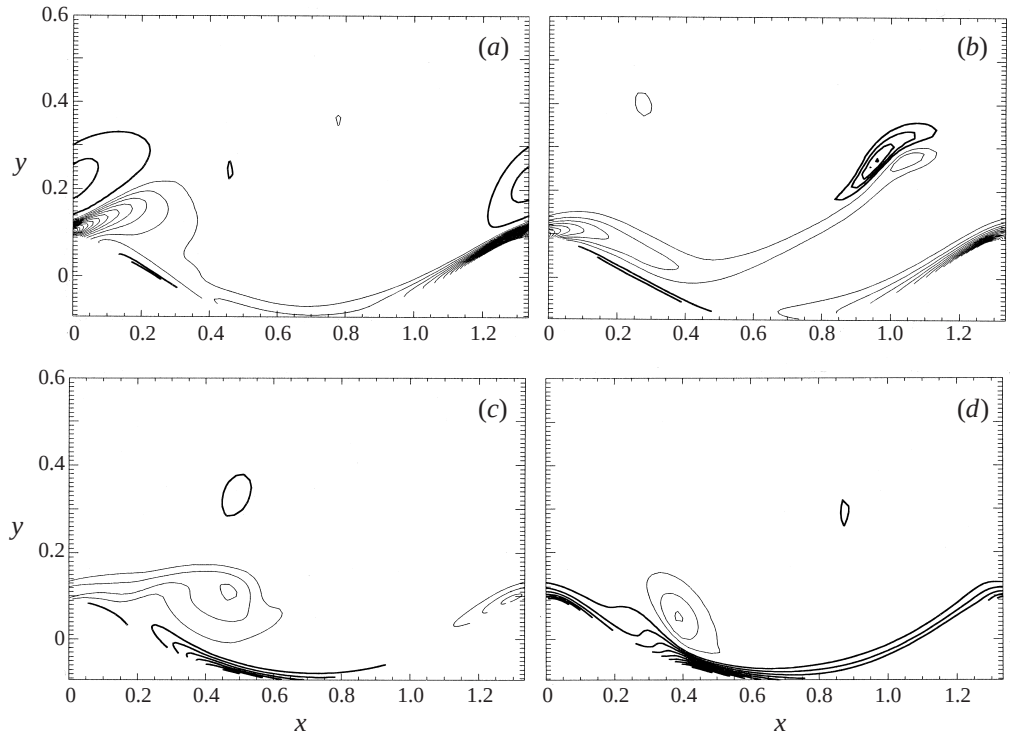

FIGURE 14. Spanwise component of vorticity ω_χ for $l = 1.333$, $h = 0.187$, $Re = 1005$, $L_\chi = 0.66$ in the plane $\chi = 0.333$, (*a*) $t = \pi/4$; (*b*) $t = \pi/2$; (*c*) $t = 3\pi/4$; (*d*) $t = \pi$ ($\Delta\omega_\chi = 6$).

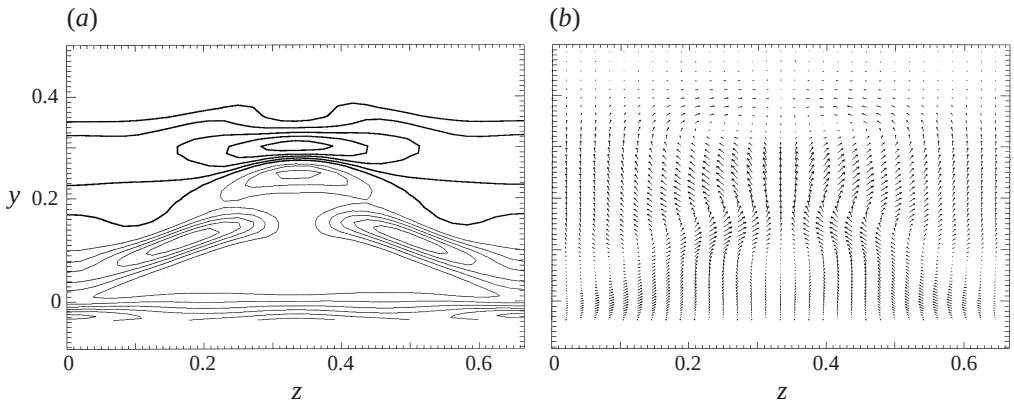

FIGURE 15. (*a*) Spanwise component of vorticity ω_χ at $t = \pi/2$ for $l = 1.333$, $h = 0.187$, $Re = 1005$, $L_\chi = 0.66$ in the plane $x = 1$ ($\Delta\omega_x = 3.5$). (*b*) Flow at $t = \pi/2$ in the plane $x = 1$ for $l = 1.333$, $h = 0.187$, $Re = 1005$, $L_\chi = 0.66$.

the bottom and create a sort of sediment jet in the centre of the computational box.

Since the size of the three-dimensional vortex structure which is originated by the instability of two-dimensional flow is equal to the width L_χ of the computational box, the results obtained cannot be assumed to describe the actual flow field. A further

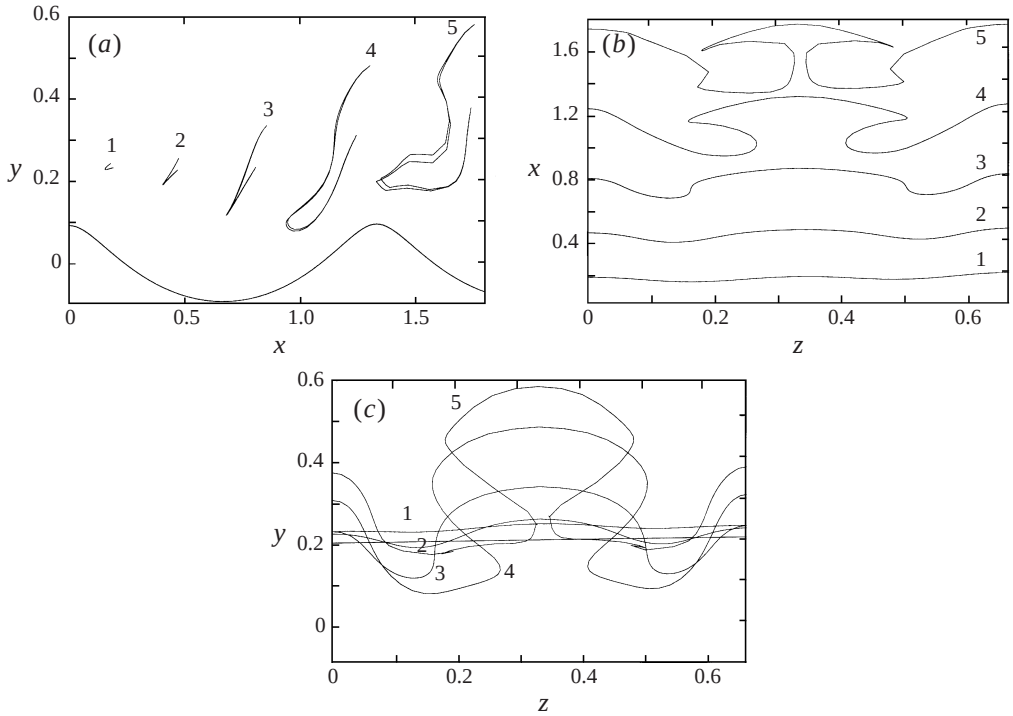

FIGURE 16. Subsequent locations of passive tracers released just above the crest at $t_i = 28\pi$ for $l = 1.333$, $h = 0.187$, $Re = 1005$, $L_\chi = 0.66$. (1) $t = t_i + \pi/8$; (2) $t = t_i + \pi/4$; (3) $t = t_i + 3\pi/8$; (4) $t = t_i + \pi/2$; (5) $t = t_i + 5\pi/8$.

simulation was performed for the same values of the parameters but fixing $L_\chi = 3.3$ and introducing an initial perturbation of small amplitude but with many periodic components in the χ-direction. Moreover, the value of N_χ was increased from 32 to 100. In this new simulation, the χ-dependence of the solution is no longer regular. From figure 17, where the streamwise component of vorticity is plotted in a plane parallel to the ripple surface and in the vertical plane $x = 0$, the appearance of vorticity streaks is evident. The velocity which is induced in the vertical direction by these vortex structures tends to carry slow fluid from the wall towards the irrotational region and fluid characterized by large momentum towards the bottom, thus creating a large and efficient mixing. The establishment of a three-dimensional flow field characterized by small vortex structures has a great impact on sediment dynamics. Similarly to figure 16, figure 18 shows the subsequent locations of passive tracers released at the beginning of the cycle close to the ripple crest. Even though sediment particles are not simply convected because of their inertia and because of gravity force, figure 18 suggests that the sediments, which are piled up at the ripple crests by the action of the main two-dimensional vortex structures, are then lifted up and ejected into the flow also by the action of the three-dimensional structures, which create an additional strong mixing and hence increase dispersion effects.

5. Conclusions

Numerical simulations of Navier–Stokes and continuity equations have clarified the process by which the oscillatory flow over two-dimensional ripples attains a

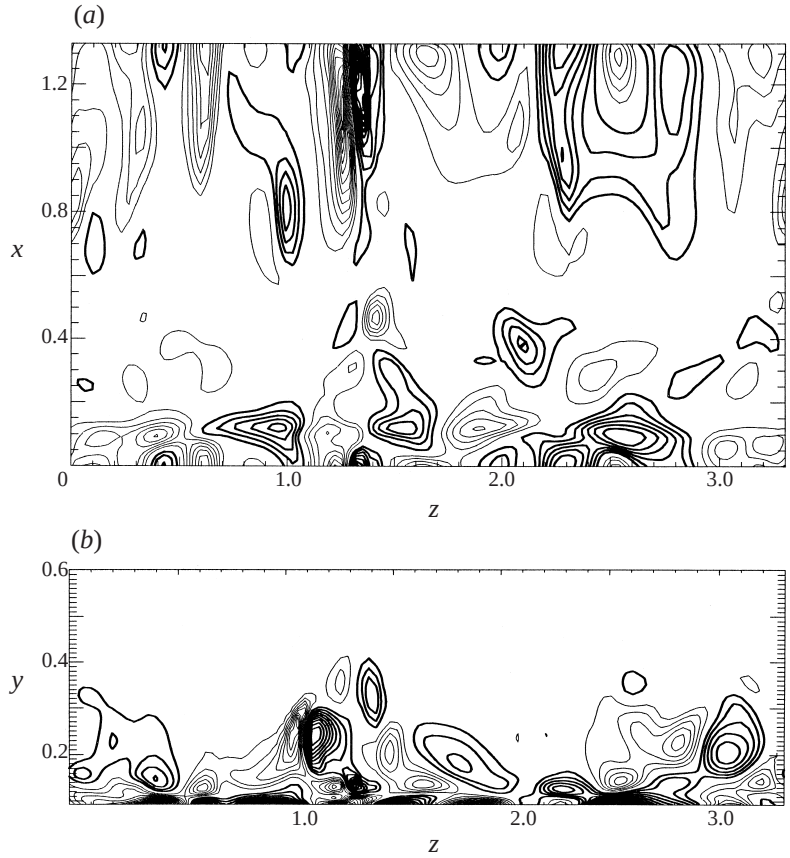

FIGURE 17. Streamwise component of vorticity ω_ξ for $l = 1.333$, $h = 0.187$, $Re = 875$, $L_\chi = 3.3$ at $t = \pi/4$: (*a*) in the plane $\eta = 0.055$, ($\Delta\omega_\xi = 1$); (*b*) in the plane $x = 0$ ($\Delta\omega_0 = 1.2$).

three-dimensional configuration. In particular, the analysis by Hara & Mei (1990*a*), who considered ripples of small amplitude or weak flows, has been extended by tackling the problem for steeper ripples and stronger flows. The nonlinear terms ignored by Hara & Mei (1990*a*) have different effects depending on the values of the parameters. When fluid displacement is comparable with ripple wavelength and spatially three-dimensional subharmonic pertubations are considered, flow separation and the presence of a free shear layer have a destabilizing effect and the flow becomes more easily three-dimensional. On the other hand, when the fluid displacement is small and Taylor–Görtler vortices tend to appear, nonlinear effects make the two-dimensional flow more stable. The simulation of the three-dimensional flow for values of the paramenters characterizing actual ripples is beyond the power of present computers.

An attempt to simulate the flow over sea ripples has been performed, but only moderate values of the Reynolds number have been considered. Vorticity dynamics is characterized by the appearance of mushroom vortices originated by the three-dimensional instability of the shear layer generated by boundary layer separation at ripple crests. The appearance of three-dimensional vortex structures increases mixing processes and the flow can more easily put into suspension loose particles lying on the bottom. To understand sediment dynamics at the bottom of sea waves a Lagrangian

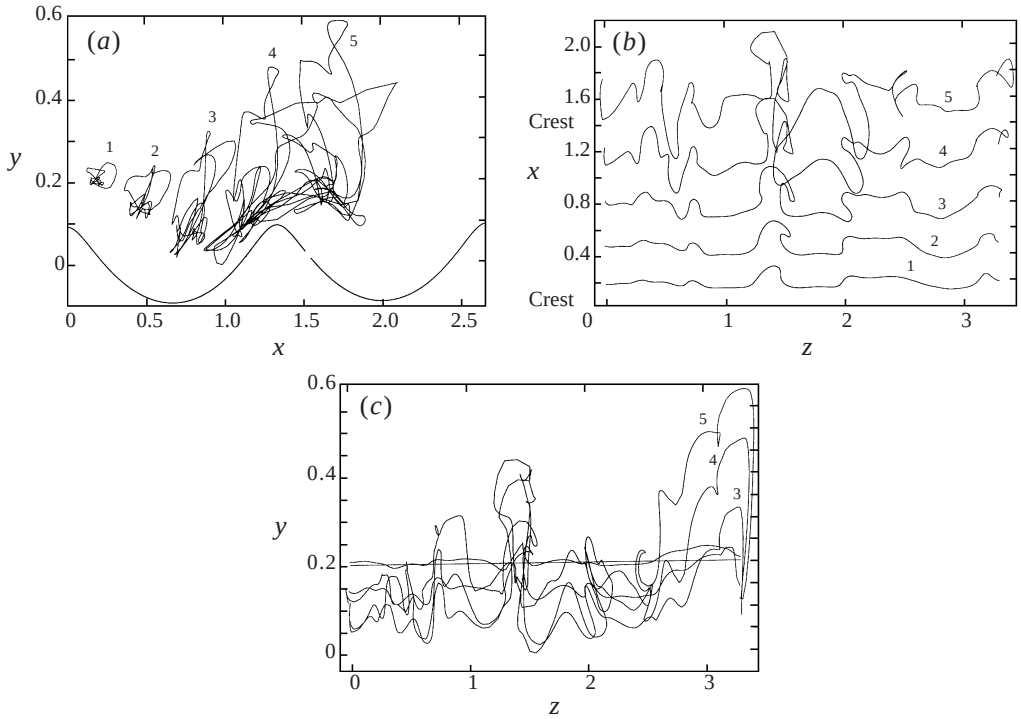

FIGURE 18. Subsequent locations of passive tracers released just above the crest at $t_i = 24\pi$ for $l = 1.333$, $h = 0.187$, $Re = 1005$, $L_\chi = 3.3$. (1) $t = t_i + \pi/8$; (2) $t = t_i + \pi/4$; (3) $t = t_i + 3\pi/8$; (4) $t = t_i + \pi/2$; (5) $t = t_i + 5\pi/8$.

simulation of the phenomenon could be attempted. However, before attempting such simulation the study of the flow over a rough wall and a moving boundary should be performed.

The financial support of the European Union through contract no. MAS3-CT97-0115 (SEDMOC) and of the Office of Naval Research through contract N00014-97-1-0790 is gratefully acknowledged. Thanks are also due to the Ministero dell'Università e della Ricerca Scientifica e Tecnologica and to the University of Genova who partially supported the research project through contracts Cofin 97 Morfodinamica fluviale e Costiera and Processi vorticosi, turbolenti, caotici – Applicazioni impiantistiche ed ambientali.

REFERENCES

AKHAVAN, R., KAMM, R. D. & SHAPIRO, A. H. 1991 An investigation of transition to turbulence in bounded oscillatory Stokes flow. Part 2. Numerical simulations. *J. Fluid Mech.* **225**, 423–444.

BATCHELOR, G. K. 1967 *An Introduction to Fluid Dynamics*. Cambridge University Press.

BLONDEAUX, P. 1990 Sand ripples under sea waves. Part 1. Ripple formation. *J. Fluid Mech.* **218**, 1–17.

BLONDEAUX, P. & VITTORI, G. 1991 Vorticity dynamics in an oscillatory flow over a rippled bed. *J. Fluid Mech.* **226**, 257–289.

BLONDEAUX, P. & VITTORI, G. 1999 Boundary layer and sediment dynamics under sea waves. *Adv. Coastal Ocean Engng* **4**, 133–190.

CRAIK, A. D. D. 1971 Non-linear resonant instability in boundary layers. *J. Fluid Mech.* **50**, 393–413.

Feigenbaum, M. J. 1978 Quantitative universality for a class of nonlinear transformation. *J. Statist. Phys.* **19**, 25–32.

Feigenbaum, M. J. 1979 The onset spectrum of turbulence. *Phys. Lett.* A **74**, 375–378.

Feigenbaum, M. J. 1980 The transition to aperiodic behaviour in turbulent systems. *Commun. Math. Phys.* **77**, 65–86.

Hall, P. 1984 On the stability of the unsteady boundary layer on a cylinder oscillating transversely in a viscous fluid. *J. Fluid Mech.* **146**, 347–367.

Hansen, E. A., Fredsøe, J. & Deigaard, R. 1994 Distribution of suspended sediment over wave generated ripples. *J. Waterway, Port, Coastal Ocean Engng* **120**, 37–55.

Hara, T. & Mei, C. C. 1990*a* Centrifugal instability of an oscillatory flow over periodic ripples. *J. Fluid Mech.* **217**, 1–32.

Hara, T. & Mei, C. C. 1990*b* Oscillating flow over periodic ripples. *J. Fluid Mech.* **211**, 183–209.

Harlow, H. & Welch, J. E. 1965 Numerical calculation of time-dependent viscous incompressible flow of fluid with free surface. *Phys. Fluids* **8**, 2182–2189.

Honji, H. 1975 Streaked flow around an oscillating circular cylinder. *J. Fluid Mech.* **69**, 229–240.

Kim, J. & Moin, P. 1985 Application of a fractional-step method to incompressible Navier–Stokes equation. *J. Comput. Phys.* **59**, 308–323.

Longuet–Higgins, M. S. 1981 Oscillating flow over steep sand ripples. *J. Fluid Mech.* **107**, 1–35.

Mei, C. C. & Liu, P. L. F. 1993 Surface waves and coastal dynamics. *Ann. Rev. Fluid. Mech.* **25**, 215–240.

Nielsen, P. 1979 Some basic concepts of wave sediment transport. *Ser. Paper* 20, *Inst. Hydrodyn. Hydraul. Engng Tech. Univ. Denmark*, 160 pp.

Orlandi, P. 1989 A numerical method for direct simulation of turbulence in complex geometries. *Annual Research Brief* 215. Center for Turbulence Research.

Sato, S., Mimura, N. & Watanabe, A. 1984 Oscillatory boundary layer flow over a rippled bed. *Proc. XIX Conf. on Coastal Engng, Houston*, pp. 2293–2309. ASCE.

Shum, K. T. 1988 A numerical study of vortex dynamics over rigid ripples. PhD thesis, MIT Dept. Civil Engng.

Sleath, J. F. A. 1974 A numerical study of the influence of bottom roughness on mass transport by water waves. In *Numerical Methods in Fluid Dynamics* (ed. C. A. Brebbia & J. J. Connor). Pentech Press.

Sleath, J. F. A. 1984 *Sea Bed Mechanics.* Wiley.

Sleath, J. F. A. & Ellis, A. C. 1978 Ripple geometry in oscillatory flow. *CUED/A – Hydraulics/TR2.* University of Cambridge. Engineering Department.

Smith, P. A. & Stansby, P. K. 1985 Wave-induced bed flows by a Lagrangian vortex scheme. *J. Comput. Phys.* **60**, 489–516.

Vittori, G. 1989 Nonlinear viscous oscillatory flow over a small amplitude wavy wall. *J. Hydraul. Res.* **27**, 267–280.

Vittori, G. & Blondeaux, P. 1991 A route to chaos in an oscillatory flow: Feigenbaum scenario. *Phys. Fluids* A **3**, 2492–2495.

Vittori, G. & Blondeaux, P. 1992 Sandy ripples under sea waves. Part 3. Brick-pattern ripple formation. *J. Fluid Mech.* **239**, 23–45.

Vittori, G. & Verzicco, R. 1998 Direct simulation of transition in an oscillatory boundary layer. *J. Fluid Mech.* **371**, 207–232.